

Quantum effects in liquid water and ice: Model dependence

Lisandro Hernández de la Peña^{a)} and Peter G. Kusalik^{b)}

Department of Chemistry, Dalhousie University, Halifax, Nova Scotia B3H 4J3, Canada

(Received 26 April 2006; accepted 30 June 2006; published online 4 August 2006)

This paper explores the influence of choice of potential model on the quantum effects observed in liquid water and ice. This study utilizes standard rigid models and a more formal context for the rigid-body centroid molecular dynamics methodology used to perform the quantum simulations is provided. Quantum and classical molecular dynamics simulations are carried out for liquid water and ice Ih at 298 and 220 K, respectively, with the simple point charge/extended and TIP4P-Ew water models. The results obtained for equilibrium and dynamical properties are compared with those recently reported on TIP4P [L. Hernández de la Peña and P. G. Kusalik, *J. Chem. Phys.* **121**, 5992 (2004); L. Hernández de la Peña *et al.*, *J. Chem. Phys.* **123**, 144506 (2005)]. For the liquid, an energy shift of about 8% and an average molecular uncertainty of about 11° were found independently of the water model. The self-diffusion coefficient consistently increases by more than 50% when going from the classical to the quantum system and quantum dynamics are found to reproduce the experimental isotopic shifts with the models examined. The ice results compare remarkably well with those previously reported for the TIP4P water model; they confirm that quantum effects are considerable and that the quantum mechanical uncertainty and the energy shifts due to quantization are smaller in ice than in liquid water. The relevance of these findings in the context of the construction of water models is briefly discussed. © 2006 American Institute of Physics. [DOI: 10.1063/1.2238861]

I. INTRODUCTION

A variety of simulation techniques have been applied to calculate equilibrium and dynamical properties of water. Among them, path integral methods^{1–4} have played a very important role allowing the simulation of quantum liquid water^{5–10} and quantum ice.¹¹ Path integral simulations address directly the impact of the quantum mechanical uncertainty of the proton in the properties of water in condensed phase. Although only equilibrium and structural properties were available in early work, approximations were later developed to solve the quantum dynamics. These approximate techniques include the Feynman-Hibbs variational approach,¹ the centroid molecular dynamics (CMD) method,^{12–18} and the very recently proposed linearized path integral description,¹⁹ where these have been applied to flexible molecular models of water in liquid simulations.^{9,10,19}

Recently, the analysis of dynamical quantum effects with rigid water models has become possible with the implementation of the CMD method for rigid bodies.^{20–24} This technique has permitted the simulation of light and heavy liquid water,^{21–23} as well as ice Ih,²⁴ all carried out with the TIP4P (Ref. 25) model. The results have indicated that the rigid-body CMD method captures the true dynamics better than a classical simulation and that the impact of quantization on the dynamics is very large [about 50% (Ref. 21)]. The isotopic shift of the calculated energy and self-diffusion coeffi-

cients compared remarkably well with previous path integral simulations and experiment.^{5–10} Another important finding was that the quantum mechanical uncertainty in liquid water was larger than the one found in TIP4P ice Ih at about the same temperature,²³ indicating the critical importance of the local environment in this property of liquid water. Other results²² based on this water model have indicated that while quantization is important for liquid water at 25 °C, it becomes more important at lower temperatures. In addition, a very recent study²⁶ with the simple point charge/extended (SPC/E) model and the ring polymer molecular dynamics method found that quantization decreases the liquid water viscosity by about one-third. A rigid-body CMD study of TIP4P ice Ih (Ref. 24) over a range of temperatures, which also probed its melting process, found quantum effects to be significant.

The study of liquid water and ice remains an active field of research. After more than three decades of water simulations a large number of water models have been proposed, among which empirical rigid-body potentials continue to be the most widely used. Although such potential models have proven to be quite successful given their simplicity, their limitations are also recognized. Their inability to reproduce experimental results has been assigned to various factors, including the absence of vibrations, the absence of polarizability, and their electronic parametrization. However, in moving beyond empirical potentials, the results reviewed above suggest that a major improvement in the description of water structure and dynamics takes place when the quantum proton uncertainty is taken into account. Therefore, it is important to verify that these findings are not specific to the

^{a)}Also at Chemical Physics Theory Group, Department of Chemistry, University of Toronto, Toronto, Ontario, Canada.

^{b)}Also at Department of Chemistry, University of Calgary, Calgary, Alberta T2N 1N4, Canada.

TIP4P water model, but in fact, sufficiently general and representative for other models and perhaps real water.

In this paper, the application of the CMD method to rigid bodies is revisited. A general centroid constraint function is derived and its use in the evaluation of orientational centroid constrained path integrals is presented. We examine the dependence of the isotopic effects on the choice of the water model by carrying out quantum simulations with two rigid water models, the SPC/E (Ref. 27) and TIP4P-Ew (Ref. 28) potentials. We demonstrate that, independent of the choice of rigid model, quantum effects in liquid water at 298 K are large and that the approximate quantum dynamics accurately reproduce the experimental isotopic shift of the diffusion coefficients. We also report results for classical and quantum ice Ih at 220 K for these two water models and verify that the quantum mechanical uncertainty in liquid water is larger than in ice Ih. Finally, the implications of these findings to water modeling is discussed.

The paper is organized as follows. Section II reviews the application and implementation of the CMD method in rigid-body systems. Section III discusses the simulation details, the results are presented in Sec. IV, and our conclusions are given in Sec. V.

II. CMD FOR RIGID BODIES

A. Theoretical background

The partition function of a rigid quantum object (i.e., molecule) with a relatively large mass m and small inertia moments $(I_x, I_y, I_z) = \text{diag}(\mathbf{I})$ in an external potential $U(\mathbf{R}, \mathbf{\Omega})$ can be written in path integral form as^{1,2}

$$Z = \left(\frac{m}{2\pi\beta\hbar^2} \right)^{3/2} \int d\mathbf{R} \int_{\mathbf{\Omega}(0)=\mathbf{\Omega}(\beta\hbar)} \mathcal{D}\mathbf{\Omega}(\tau) \times \exp\left(-\frac{1}{\hbar} S[\mathbf{R}, \mathbf{\Omega}(\tau)] \right), \quad (1)$$

where

$$S[\mathbf{R}, \mathbf{\Omega}(\tau)] = \int_0^{\beta\hbar} \left(\frac{1}{2} \mathbf{I}(\tau) \dot{\mathbf{\Omega}}^2(\tau) + U[\mathbf{R}, \mathbf{\Omega}(\tau)] \right) d\tau. \quad (2)$$

Here, $\int_{\mathbf{\Omega}(0)=\mathbf{\Omega}(\beta\hbar)} \mathcal{D}\mathbf{\Omega}(\tau)$ is a closed integration over the orientational paths $\mathbf{\Omega}(\tau)$, \mathbf{R} is the position of the molecular center of mass, $(1/2)\mathbf{I}\dot{\mathbf{\Omega}}^2$ is the kinetic energy of the orientational path, and $\beta = 1/kT$. For notational simplicity we will refer to a single quantum molecule, where the generalization to a many-body system is straightforward.

The molecular orientations that make up $\mathbf{\Omega}(\tau)$ can be represented by a rotation matrix, three Euler angles, or a unit quaternion $\tilde{q}(\tau)$; however, there are some specific advantages associated with using quaternions in what follows. Since the quaternion parameters²⁹ map three-dimensional rotations onto a four-dimensional sphere, then given a particular closed path $\mathbf{\Omega}(\tau)$ and a specified orientation $\mathbf{\Omega}_c \equiv \tilde{q}_c$, we can define the function

$$G(\mathbf{\Omega}_c) \equiv G(\tilde{q}_c) = \int_0^{\beta\hbar} \Gamma^2(\tau) d\tau = 4 \int_0^{\beta\hbar} \arccos^2(\tilde{q}(\tau) \cdot \tilde{q}_c) d\tau, \quad (3)$$

where $\tilde{q}(\tau) \cdot \tilde{q}_c$ can be regarded as the inner product between two four-dimensional unit vectors. It is clear that Γ is the rotation angle or curved distance between the orientations $\tilde{q}(\tau)$ and \tilde{q}_c . Since the gradient of $G(\tilde{q}_c)$ is given by

$$\nabla_{\tilde{q}_c} G(\tilde{q}_c) = \int_0^{\beta\hbar} \frac{2\Gamma(\tau)}{\sin(\Gamma(\tau)/2)} [\tilde{q}(\tau) - \tilde{q}_c(\tilde{q}_c \cdot \tilde{q}(\tau))] d\tau, \quad (4)$$

it is then convenient to introduce

$$\sigma(\tilde{q}_c) = -\frac{1}{2\alpha} \nabla_{\tilde{q}_c} G(\tilde{q}_c) \quad (5)$$

$$= \tilde{q}_c - \frac{1}{\alpha} \int_0^{\beta\hbar} \frac{\Gamma(\tau)}{\sin(\Gamma(\tau)/2)} \tilde{q}(\tau) d\tau, \quad (6)$$

where

$$\alpha = \int_0^{\beta\hbar} \frac{\Gamma(\tau)}{\tan(\Gamma(\tau)/2)} d\tau. \quad (7)$$

Defining the average orientation \tilde{q}_0 of the path $\tilde{q}(\tau)$ as the minimum of $G(\tilde{q}_c)$, one then immediately obtains from Eq. (5) that $\sigma(\tilde{q}_0) = 0$. It should be noted that, since $G(\tilde{q}_c)$ is a continuous function and because of the compactness of its domain (the four-dimensional sphere), \tilde{q}_0 always exist. It can be also shown³⁰ that if the whole path is located in a “hemisphere,” \tilde{q}_0 is unique.

From Eqs. (6) and (7) it is easily verified that for a path that remains close to \tilde{q}_c (i.e., near the classical limit) one recovers a result that resembles the usual definition of the centroid variable, since

$$\lim_{\Gamma(\tau) \approx 0} \sigma(\tilde{q}_c) = \tilde{q}_c - \frac{1}{\beta\hbar} \int_0^{\beta\hbar} \tilde{q}(\tau) d\tau = \tilde{q}_c - \tilde{q}_0. \quad (8)$$

Clearly, this result is only valid when the curvature of the orientational space becomes negligible.

Representing the orientational imaginary time paths $\mathbf{\Omega}(\tau)$ in centroid form we obtain

$$Z = \left(\frac{m}{2\pi\beta\hbar^2} \right)^{3/2} \int d\mathbf{R} \int d\mathbf{\Omega}_c \rho_c(\mathbf{R}, \mathbf{\Omega}_c), \quad (9)$$

where

$$\rho_c(\mathbf{R}, \mathbf{\Omega}_c) = \int_{\mathbf{\Omega}(0)=\mathbf{\Omega}(\beta\hbar)} \mathcal{D}\mathbf{\Omega}(\tau) \delta(\sigma(\mathbf{\Omega}_c)) \times \exp\left\{ -\frac{1}{\hbar} S[\mathbf{R}, \mathbf{\Omega}(\tau)] \right\}, \quad (10)$$

$S[\mathbf{R}, \mathbf{\Omega}(\tau)]$ is given by Eq. (2) and $\sigma(\mathbf{\Omega}_c) \equiv \sigma(\tilde{q}_c)$ is given by Eq. (6). From Eq. (9) one can write a centroid potential of mean force as

$$V_c(\mathbf{R}, \mathbf{\Omega}_c) = -\frac{1}{\beta} \ln(\rho_c(\mathbf{R}, \mathbf{\Omega}_c)). \quad (11)$$

The centroid molecular dynamics method prescribes a time evolution of the centroid variable on this potential surface according to the following centroid force and torque:

$$\mathbf{F}_c(\mathbf{R}, \mathbf{\Omega}_c) = -\nabla_{\mathbf{R}} V_c(\mathbf{R}, \mathbf{\Omega}_c) \quad (12)$$

and

$$\mathbf{T}_c(\mathbf{R}, \mathbf{\Omega}_c) = -\nabla_{\mathbf{\Omega}_c} V_c(\mathbf{R}, \mathbf{\Omega}_c). \quad (13)$$

The resulting centroid dynamics can then be used to calculate equilibrium and approximate dynamical information of the quantum system.

B. Implementation

Since the centroid evolves classically on the potential $V_c(\mathbf{R}, \mathbf{\Omega}_c)$, the real time dynamics is no more difficult than a conventional MD simulation of rigid bodies with center of mass and orientational equations of motion. However, according to Eqs. (10)–(13) the centroid evolution requires the evaluation of an orientationally constrained path integral.

In practice, the path integral in Eq. (10) is discretized as³¹

$$\rho_c(\mathbf{R}, \mathbf{\Omega}_c) \approx \left(\frac{P}{2\pi\beta\hbar^2} \right)^{3P/2} \prod_{k=1}^P I_k^{3/2} \int d\mathbf{\Omega}_k \delta(\sigma(\mathbf{\Omega}_c)) \times \exp\{-\beta\Phi(\mathbf{R}, \mathbf{\Omega}_k)\}, \quad (14)$$

where

$$\Phi(\mathbf{R}, \mathbf{\Omega}_k) = \frac{I_k P}{2\beta^2 \hbar^2} \Theta^2(\mathbf{\Omega}_k, \mathbf{\Omega}_{k+1}) + \frac{1}{P} U(\mathbf{R}, \mathbf{\Omega}_k), \quad (15)$$

with $\mathbf{\Omega}_{P+1} = \mathbf{\Omega}_1$. In these equations, $\Theta(\mathbf{\Omega}_k, \mathbf{\Omega}_{k+1})$ is the rotation angle between orientations k and $k+1$, and I_k is the inertia moment associated with that rotation. Thus, Eqs. (12) and (13) become

$$\mathbf{F}_c(\mathbf{R}, \mathbf{\Omega}_c) = \frac{-1}{\rho_c(\mathbf{R}, \mathbf{\Omega}_c)} \left(\frac{P}{2\pi\beta\hbar^2} \right)^{3P/2} \prod_{k=1}^P I_k^{3/2} \int d\mathbf{\Omega}_k \times \delta(\sigma(\mathbf{\Omega}_c)) \left(\frac{1}{P} \sum_{s=1}^P \nabla_{\mathbf{R}} U(\mathbf{R}, \mathbf{\Omega}_s) \right) \times \exp\{-\beta\Phi(\mathbf{R}, \mathbf{\Omega}_k)\} \quad (16)$$

and

$$\mathbf{T}_c(\mathbf{R}, \mathbf{\Omega}_c) = \frac{-1}{\rho_c(\mathbf{R}, \mathbf{\Omega}_c)} \left(\frac{P}{2\pi\beta\hbar^2} \right)^{3P/2} \prod_{k=1}^P I_k^{3/2} \int d\mathbf{\Omega}_k \times \delta(\sigma(\mathbf{\Omega}_c)) \left(\frac{1}{P} \sum_{s=1}^P \nabla_{\mathbf{\Omega}_s} \Phi(\mathbf{R}, \mathbf{\Omega}_s) \right) \times \exp\{-\beta\Phi(\mathbf{R}, \mathbf{\Omega}_k)\}. \quad (17)$$

In this discretized picture, the centroid constraint transforms into

$$\sigma(\mathbf{\Omega}_c) = \tilde{q}_c - \frac{1}{\alpha} \sum_{k=1}^P \frac{\Gamma_k}{\sin(\Gamma_k/2)} \tilde{q}_k, \quad (18)$$

with

$$\alpha = \frac{1}{P} \sum_{k=1}^P \frac{\Gamma_k}{\tan(\Gamma_k/2)}. \quad (19)$$

Due to the quaternion normalization condition, the constraint Eq. (18) has a redundant degree of freedom which can be associated with the scalar component of this equation by setting the centroid to be $\tilde{q}_c = (1; 0, 0, 0) = \tilde{1}$. Thus, using the polar representation of a unit quaternion $\tilde{q}_k = (q_k^{(0)}; \mathbf{q}_k) = (\cos(\theta_k/2); \sin(\theta_k/2)\mathbf{u}_k)$, Eq. (18) becomes $\sigma(\tilde{1}) = (0; \boldsymbol{\sigma})$ with the vector component given by

$$\boldsymbol{\sigma} = - \sum_{k=1}^P \frac{\theta_k}{\sin(\theta_k/2)} \mathbf{q}_k = - \sum_{k=1}^P \theta_k \mathbf{u}_k. \quad (20)$$

This equation can be used to calculate a quaternion \tilde{q}_l as a function of the $P-1$ remaining quaternions, such that $\tilde{q}_0 = \tilde{q}_c = \tilde{1}$, that is,

$$\theta_l = \left| \sum_{k \neq l}^P \theta_k \mathbf{u}_k \right| \quad (21)$$

and

$$\mathbf{u}_l = \left(\frac{-1}{\theta_l} \right) \sum_{k \neq l}^P \theta_k \mathbf{u}_k. \quad (22)$$

It is easily verified that for $P=2$ and $P=3$ one obtains the “two-bead” and “three-bead” formulas given in Ref. 20.

A natural way of evaluating the constrained path integral in Eqs. (16) and (17) is with the Monte Carlo method. One could first generate $P-1$ random orientational displacements and then evaluate the remaining orientational displacement according to Eqs. (21) and (22). Denoting an initial P -bead configuration as $(\tilde{q}_1, \dots, \tilde{q}_P) \equiv \tilde{Q}_P$, the new configuration \tilde{Q}'_P is accepted with a probability $p(\tilde{Q}_P \rightarrow \tilde{Q}'_P)$ given by

$$p(\tilde{Q}_P \rightarrow \tilde{Q}'_P) = \min\{1, \exp(-\beta\Delta\Phi)\}, \quad (23)$$

where

$$\Delta\Phi = \sum_{k=1}^P (\Phi(\mathbf{R}, \tilde{q}'_k) - \Phi(\mathbf{R}, \tilde{q}_k)). \quad (24)$$

By this means, one can generate a set of configurations $(\tilde{Q}_P^{(1)}, \dots, \tilde{Q}_P^{(n)})$ over which to average the forces and torques according to Eqs. (16) and (17).

It is also possible to obtain a set of bead configurations via MD. In this approach, an artificial bead dynamics along the *timelike* variable ξ is generated by providing an initial kinetic energy \mathcal{K} [see Eq. (15)],

$$\mathcal{K} = \sum_{k=1}^P \left(\frac{L_{x,k}^2}{2I'_x} + \frac{L_{y,k}^2}{2I'_y} + \frac{L_{z,k}^2}{2I'_z} \right), \quad (25)$$

and evolving the bead orientations according to the appropriate potential $\Phi(\mathbf{R}, \mathbf{\Omega}_k)$, together with the corresponding con-

straint equations to enforce the centroid conservation. This centroid constrained dynamics could, in principle, be implemented in several ways. The constraint equations could be used to eliminate the redundant degrees of freedom of the system such that the dynamics evolve only the relevant variables which implicitly include the constraints. In this case, in particular, one can use Eqs. (21) and (22) and express the time evolution of bead l as a function of the remaining $P-1$ beads; i.e., $\tilde{q}_l(\xi) = f(\dots, \tilde{q}_k(\xi), \dots)$ where $l \neq k$. Finally, the $P-1$ explicitly evolving orientations need to be coupled to a Nose-Hoover thermostat³² such that canonical sampling is achieved.

Defining the total torque acting on bead k as $\mathbf{T}_k = -\nabla_{\tilde{\mathbf{q}}_k} \Phi(\mathbf{R}, \mathbf{\Omega}_k)$, the rotational equations of motion for bead k in its principal frame would then be given as

$$\dot{\tilde{\mathbf{q}}}_k = \frac{1}{2} \tilde{\mathbf{q}}_k \cdot \tilde{\mathbf{w}}_k, \quad (26)$$

$$\dot{\mathbf{L}}_k = \mathbf{T}_k - \mathbf{w}_k \times \mathbf{L}_k - \lambda_{k,1} \mathbf{L}_k, \quad (27)$$

$$\dot{\lambda}_{k,1} = \frac{1}{\mathcal{F}_1} \left[\mathcal{K} - \frac{3(P-1)}{\beta} \right] - \lambda_{k,1} \lambda_{k,2}, \quad (28)$$

$$\dot{\lambda}_{k,j} = \frac{1}{\mathcal{F}_j} \left[\mathcal{F}_{j-1} \lambda_{k,j-1}^2 - \frac{1}{\beta} \right] - \lambda_{k,j} \lambda_{k,j+1}, \quad (29)$$

$$\dot{\lambda}_{k,M} = \frac{1}{\mathcal{F}_M} \left[\mathcal{F}_{M-1} \lambda_{k,M-1}^2 - \frac{1}{\beta} \right], \quad (30)$$

where Eq. (26) is written in quaternion form with $\tilde{\mathbf{w}}_k = (0; \mathbf{w}_k)$ being the quaternion representation of the angular velocity vector \mathbf{w}_k , $\lambda_{k,j}$ are the parameters of a Nose-Hoover chain thermostat of length M (Ref. 21) coupled to the dynamics of bead k . $\mathcal{F}_1 = 3(P-1)\kappa^2/\beta$ and $\mathcal{F}_j = \kappa^2/\beta$ for $2 \leq j \leq M$, with κ as the characteristic relaxation time of the Nose-Hoover bath. We note that the use of this thermostating scheme greatly improves the efficiency of the path integral evaluation and enforces the required canonical sampling. The equations of motion can be integrated with a predictor-corrector algorithm or with more recent and efficient integrators.³³

It is clear that the evaluation of the path integral is a crucial part of the CMD implementation. In principle, well converged values of the centroid force and centroid torque are needed in order to propagate the centroid; such an approach has been called the *primitive* algorithm.⁹ Introducing the “instantaneous” centroid torque, $\mathbf{t}_c = (1/P) \sum_{k=1}^P \mathbf{T}_k$, then from Eq. (17) we formally have

$$\mathbf{T}_c(\mathbf{R}, \mathbf{\Omega}_c) = \lim_{\nu \rightarrow \infty} \frac{1}{\nu} \sum_{n=1}^{\nu} \mathbf{t}_c(\tilde{\mathbf{Q}}_P^{(n)}) \quad (31)$$

$$= \lim_{\eta \rightarrow \infty} \frac{1}{\eta} \int_0^{\eta} \mathbf{t}_c(\xi) d\xi, \quad (32)$$

where the first and second equalities refer to Monte Carlo (MC) and MD evaluations, respectively, and analogous equations can be written for the centroid force. Clearly, the primi-

tive algorithm is a numerical implementation of the above equations.

Alternatively, one can use the *adiabatic* algorithm,⁹ where the centroid propagation is carried out with a relatively small Δt and only a few bead configurations are visited at each centroid phase point. In this approach the averaging then occurs on the fly. Although both MC or MD can be used to evaluate the path integral, the MD approach seems perhaps better suited to this implementation.

Although the MD algorithm described above is in general correct, it has two important limitations. First, the constrained dynamics is non-Hamiltonian³⁴ and the phase space compressibility factor associated with the invariant measure seems to be difficult to calculate. Second, the algorithm evolves only $P-1$ beads and the full effect of the constraint lies exclusively on one bead (bead l), something that may be expected to lead to nonergodic behavior. Ideally, one would like to perform a Hamiltonian dynamics where the constraint is enforced similarly in all beads, however, this would imply the complicated task of reformulating the dynamics over new (and nontrivial) orientational variables.

An alternative approach is to devise an approximate, but efficient, scheme where the constraint is conserved while ergodicity is guaranteed. Perhaps the simplest such scheme is to request that the total angular momentum of a set of beads is zero in centroid frame,³⁵ i.e.,

$$\mathbf{L}(\xi) = \sum_{k=1}^P \mathbf{L}_k(\xi) = 0. \quad (33)$$

With this requirement in place, and defining $\mathbf{t}_k = \mathbf{T}_k - \mathbf{t}_c$, the rotational equations of motion for *all* $\tilde{\mathbf{q}}_k$ follow Eqs. (26)–(30) with $\dot{\mathbf{L}}_k$ in principal frame given by

$$\dot{\mathbf{L}}_k = \mathbf{t}_k - \mathbf{w}_k \times \mathbf{L}_k - \lambda_{k,1} \mathbf{L}_k + \mathbf{S}. \quad (34)$$

The vector \mathbf{S} is calculated in centroid (or fixed) frame as

$$\mathbf{S} = \frac{1}{P} \sum_{k=1}^P \lambda_{k,1} \mathbf{L}_k, \quad (35)$$

and ensures the preservation of the total angular momentum in the thermostated dynamics. We note that by construction we have

$$\sum_{k=1}^P \mathbf{t}_k = 0, \quad (36)$$

in centroid frame. The centroid constraint is then enforced step by step via Eqs. (21) and (22) where \tilde{q}_l is chosen randomly at each step. We have previously verified numerically²⁰ that this dynamics produces converged values of the centroid force and centroid torque while conserving the centroid.

III. SIMULATION DETAILS

In this work the classical MD simulations were carried out in a standard manner.²¹ The equations of motions are integrated with a fourth order predictor-corrector algorithm with rotations represented by quaternion parameters. A

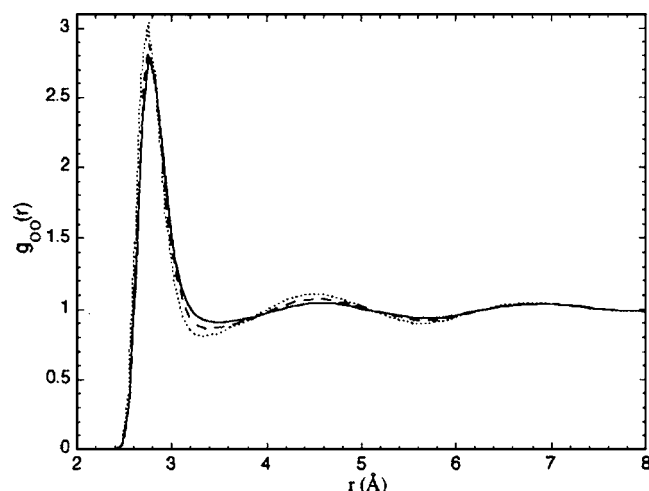


FIG. 1. Oxygen-oxygen radial distribution function of liquid SPC/E water at 298 K. The dotted, solid, and dashed lines correspond to the classical, quantum H₂O, and quantum D₂O results, respectively.

Gaussian thermostat³⁶ was used to control the system temperature. The long-range interactions are evaluated with Ewald sums. For the case of classical ice simulations, we have started with an experimentally determined lattice configuration and have carried out runs as described in Ref. 24.

The quantum simulations of liquid water were carried out with parameters identical to those used for the TIP4P model in Ref. 21 (and the method of parametrization has also been presented there); their values are $P=5$, $M=4$, $\eta=3$, $\Delta\xi=0.5$ fs, and $\Delta t=0.125$ fs (where the notation has been established in Sec. II B). It is noted that the value of κ is conveniently adjusted for the particular values of the inertia moment in the fictitious dynamics (which are in general different from the real inertia moment values of the molecule). These same parameter values were tested for quantum TIP4P ice Ih (the results have been given in Ref. 24) and they were also found to be optimal.

IV. RESULTS

This section discusses the results obtained in classical and quantum simulations of liquid water and ice. The liquid water results are presented first and include the equilibrium and dynamical properties of light and heavy water at 298 K. This is followed by the results on static properties as well as the lattice dynamics of ice Ih at 220 K.

A. Liquid water at 298 K

Figure 1 shows the oxygen-oxygen radial distribution functions (RDFs) obtained in classical and quantum simulations of light and heavy SPC/E water. The result for classical D₂O coincides with classical H₂O and is not shown. One observes that the classical system is more structured, followed by quantum D₂O and the least structured quantum H₂O system. A comparison with Fig. 5 in Ref. 21 indicates that the effect of quantization is qualitatively extremely similar. This observation is further confirmed with the oxygen-hydrogen RDF for SPC/E presented in Fig. 2. In this figure (which can be compared with Fig. 6 in Ref. 21) we observe

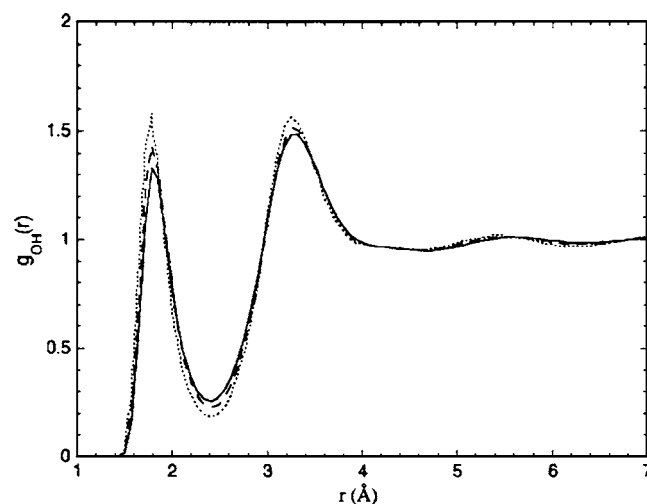


FIG. 2. Oxygen-hydrogen radial distribution function of liquid SPC/E water at 298 K. The dotted, solid, and dashed lines correspond to the classical, quantum H₂O, and quantum D₂O results, respectively.

the classical system to be the most structured and the quantum H₂O the least structured, with the quantum D₂O liquid in between. These results for the oxygen-oxygen and oxygen-hydrogen RDFs are in very good agreement with those of del Buono *et al.*⁷ for SPC water obtained via path integral molecular dynamics. It should be emphasized in this context that the CMD method generates exact equilibrium averages provided that the system is ergodic.¹⁸ The oxygen-oxygen and oxygen-hydrogen radial distribution functions for TIP4P-Ew qualitatively confirm the results of Figs. 1 and 2 (and are not shown). It should also be noted that the H₂O/D₂O (intermolecular) structural changes predicted by the present simulations have recently been shown to agree well with those extracted from x-ray diffraction experiments³⁷ on water. We remark that these relative structural changes are the most relevant test of the results presented here.

A quantitative analysis of the model dependence can be carried out on values of the intermolecular potential energies, relative energy shifts, and average molecular uncertainties. The latter values, representing the average quantum dispersion in the molecular orientations, were calculated as follows.^{21,23} First we define an instantaneous molecular uncertainty [i.e., for a particular $\bar{Q}_P^{(n)}$ bead configuration] as $\vartheta(\bar{Q}_P^{(n)}) = (1/P) \sum_{k=1}^P \theta_k^{(n)}$, and the molecular uncertainty associated with the centroid as [cf. Eq. (31)]

$$\theta_c(\mathbf{R}, \mathbf{\Omega}_c) = \lim_{\nu \rightarrow \infty} \frac{1}{\nu} \sum_{n=1}^{\nu} \vartheta(\bar{Q}_P^{(n)}). \quad (37)$$

The average molecular uncertainties in Table I are then given by³⁸

$$\langle \theta_c \rangle_c = \frac{1}{Z} \left(\frac{m}{2\pi\beta\hbar^2} \right)^{3/2} \int d\mathbf{R} \int d\mathbf{\Omega}_c \times \rho_c(\mathbf{R}, \mathbf{\Omega}_c) \theta_c(\mathbf{R}, \mathbf{\Omega}_c), \quad (38)$$

where a further integration over all molecules in the system is carried out.

TABLE I. Energy, relative energy shift, and quantum molecular uncertainty (see text) values for the SPC/E and TIP4P-Ew water models at 298 K. Results for TIP4P, included for comparison, are taken from Ref. 21.

Model	System	Energy (kJ/mol)	Relative shift (%)	Quantum uncertainty (deg)
SPC/E	Classical	-45.93	...	0
	Quantum H ₂ O	-42.33	7.8	10.7
	Quantum D ₂ O	-43.48	5.3	8.5
TIP4P-Ew	Classical	-45.99	...	0
	Quantum H ₂ O	-42.11	8.4	11.0
	Quantum D ₂ O	-43.58	5.2	8.9
TIP 4P	Classical	-41.05	...	0
	Quantum H ₂ O	-37.43	8.8	11.3
	Quantum D ₂ O	-38.63	5.9	8.9

Table I reports values obtained for the intermolecular potential energy, relative energy shifts, and average molecular uncertainties for the SPC/E and TIP4P-Ew water models and includes the results for TIP4P from Ref. 21. The results indicate that the TIP4P-Ew and SPC/E models show a slightly smaller quantum shift in the energy than was found for TIP4P. The values calculated for the TIP4P-Ew water model are generally closer to the values of the TIP4P potential. This result is reasonable considering that the TIP4P-Ew (Ref. 28) model is more similar to TIP4P (Ref. 25) than is the SPC/E (Ref. 27) model. It is also interesting to note that the estimated values of the molecular uncertainty for TIP4P-Ew and SPC/E are slightly smaller than the one determined previously for TIP4P. Furthermore, it is reasonable to expect that the smaller the molecular uncertainty, the smaller the quantum effects in the energy should be. This expectation is confirmed by comparing the values of molecular uncertainty for light water presented in Table I. The energy shifts in quantum D₂O, which are smaller, appear less dependent on the estimated molecular uncertainty. We note that while properties such as the pressure and dielectric constant were examined, it is not possible to quantify the effects

of quantization due to the relatively large errors associated with these quantities. Qualitatively, it appears that quantization somewhat increases the pressure (at fixed density) and leaves the dielectric constant essentially unchanged.

Table II reports the values of the self-diffusion coefficient and its components obtained in the classical and quantum simulations of liquid samples with the SPC/E and TIP4P-Ew potentials. The local frame is defined with the z axis along the molecular axis of symmetry and the x axis in the plane of the molecule. For the SPC/E model, the y component appears to have the smallest quantum H₂O/D₂O ratio, whereas in the TIP4P-Ew model it is the z component that is smallest. However, since these differences are just at the limit of the estimated errors they may well represent numerical noise. This is consistent with the fact that in the TIP4P results²¹ all the components have essentially the same quantum H₂O/D₂O ratio. Importantly, the results show that, independent of the model chosen, the H₂O/D₂O ratios of the self-diffusion coefficients calculated through quantum simulations are in much better agreement with the experimental value^{39,40} of 1.21 than the ratios determined from classical simulations. This indicates that the present quantum simulations, in comparison with the classical calculations, make a significant improvement in relation to the description of the microscopic dynamics of these systems.

The effect of quantization in the dynamics can be estimated with the ratio $D_{\text{quant}}/D_{\text{class}}$. The results obtained for SPC/E and TIP4P-Ew water are 1.56 and 1.69, respectively. These values are in very good agreement with previously reported results^{9,10,26} and with the TIP4P ratio of 1.53.²¹ This agreement is a further confirmation of the relevance of the quantum mechanical effects in the microscopic dynamics of liquid water. It is interesting to note that the $D_{\text{quant}}/D_{\text{class}}$ ratios given by the data in Table IV of Ref. 26 are consistently smaller than the value (1.56) obtained here for SPC/E water. Thus it would appear that the ring polymer molecular dynamics approach utilized in Ref. 26 does not completely capture the full effects of quantization.

Table III contains the calculated values of several relax-

TABLE II. Self-diffusion coefficients in 10^{-5} cm²/s for the SPC/E and TIP4P-Ew water models. The errors are about 1% of the reported values. Results for TIP4P, included for comparison, are taken from Ref 21.

Model	System	D	D_x	D_y	D_z
SPC/E	Classical H ₂ O	2.49	2.30	3.25	1.93
	Quantum H ₂ O	3.90	3.66	4.90	3.15
	Classical D ₂ O	2.48	2.26	3.21	1.97
	Quantum D ₂ O	3.34	3.09	4.29	2.64
	Classical H ₂ O/D ₂ O	1.00	1.02	1.01	0.98
	Quantum H ₂ O/D ₂ O	1.17	1.18	1.14	1.19
TIP4P-Ew	Classical H ₂ O	2.41	2.20	2.97	2.06
	Quantum D ₂ O	4.07	3.90	4.93	3.39
	Classical H ₂ O	2.37	2.18	2.94	1.98
	Quantum D ₂ O	3.42	3.23	4.10	2.91
	Classical H ₂ O/D ₂ O	1.02	1.01	1.01	1.04
	Quantum H ₂ O/D ₂ O	1.19	1.21	1.20	1.16
TIP4P	Classical H ₂ O/D ₂ O	1.04	1.04	1.03	1.05
	Quantum H ₂ O/D ₂ O	1.20	1.20	1.21	1.19

TABLE III. Molecular and collective (dielectric) relaxation times in ps for the SPC/E and TIP4P-Ew water models. Results for TIP4P, included for comparison, are taken from Ref. 21.

Model	System	τ_1^c	τ_2^c	τ_D
SPC/E	Classical H ₂ O	4.14±0.03	1.405±0.005	10±1
	Quantum H ₂ O	2.63±0.03	0.871±0.005	6±1
	Classical D ₂ O	4.80±0.03	1.620±0.005	12±1
	Quantum D ₂ O	3.53±0.03	1.172±0.005	10±1
	Classical D ₂ O/H ₂ O	1.16	1.15	1.2
	Quantum D ₂ O/H ₂ O	1.34	1.34	1.7
TIP4P-Ew	Classical H ₂ O	4.28±0.03	1.462±0.005	11±1
	Quantum H ₂ O	2.42±0.03	0.811±0.005	6±1
	Classical D ₂ O	4.80±0.03	1.631±0.005	10±1
	Quantum D ₂ O	3.44±0.03	1.160±0.005	9±1
	Classical D ₂ O/H ₂ O	1.12	1.12	0.9
	Quantum D ₂ O/H ₂ O	1.42	1.43	1.5
TIP4P	Classical D ₂ O/H ₂ O	1.13	1.13	1.0
	Quantum D ₂ O/H ₂ O	1.36	1.35	1.2

ation times for the SPC/E and TIP4P-Ew molecular models. The classical relaxation times are extracted from the appropriate orientational correlation functions according to $\tau_k^c = \int_0^\infty C_k^c(t) dt$, where

$$C_k^c(t) = \langle P_k[\hat{z}(t) \cdot \hat{z}(0)] \rangle, \quad (39)$$

where \hat{z} is a unit vector aligned with the molecular dipolar vector and P_k denotes the Legendre polynomial of order k . The quantum values are in turn calculated from the centroid time correlation function

$$C_k^c(t) = \langle P_k[\hat{z}_c(t) \cdot \hat{z}_c(0)] \rangle_c, \quad (40)$$

and with the use of the Fourier space relationship^{12–18}

$$\mathcal{G}(w) = \frac{\hbar w}{2} \left[\coth\left(\frac{\hbar w}{2}\right) + 1 \right] \mathcal{G}_c(w), \quad (41)$$

where $\mathcal{G}(w)$ and $\mathcal{G}_c(w)$ are the Fourier transforms of the quantum and centroid time correlation functions, respectively. The collective relaxation times τ_D are calculated analogously by using the standard relationship

$$\tau_D = \int_0^\infty \frac{\langle \mathbf{M}(t) \cdot \mathbf{M}(0) \rangle}{\langle \mathbf{M}^2(0) \rangle} dt, \quad (42)$$

where $\mathbf{M}(t)$ is the total dipole moment vector. It must be noted that, while more elaborate schemes for the computation of nonlinear quantum time correlation functions exist,⁴¹ we have used the more straightforward but approximate procedure represented by Eq. (41) (which becomes rigorously correct for linear operators). We point out also that, in contrast, the diffusion coefficients in Table II are obtained directly from the translational centroid time correlation function since no explicit quantization of the translational motion has been carried out.

The classical and quantum molecular relaxation time ratios obtained for the two models are comparable with the ones obtained for the TIP4P water potential.²¹ For the three models, the quantum ratios are significantly larger than the

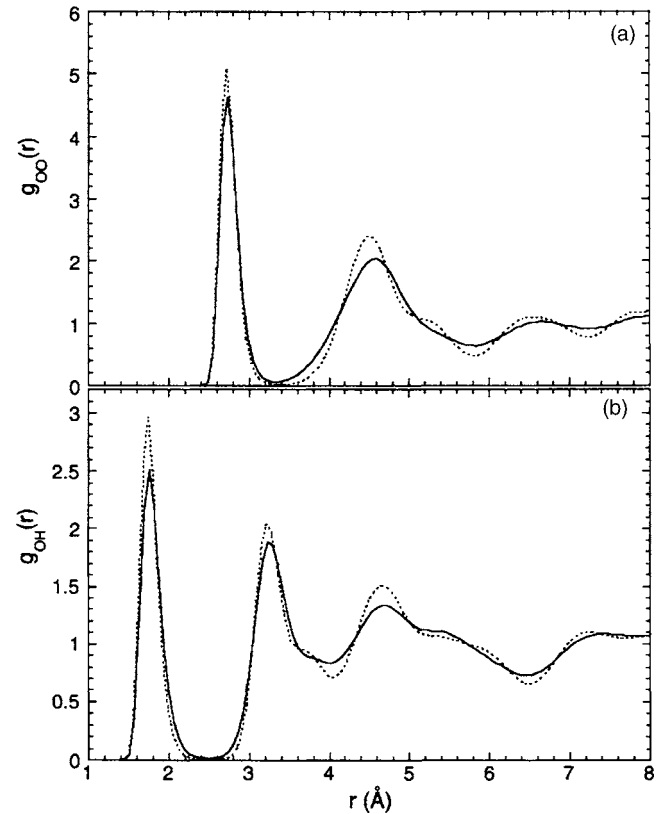


FIG. 3. Oxygen-oxygen (a) and oxygen-hydrogen (b) radial distribution functions of SPC/E ice Ih at 220 K. The results represented by dotted and solid lines correspond to the classical and quantum simulations, respectively.

classical ones, in agreement with the expected faster dynamics in the quantum system. Once again, quantization significantly increases the relaxation dynamics of the system, in agreement with the results reported previously for TIP4P (Ref. 21) and SPC/E water.²⁶

B. Ice Ih at 220 K

Figure 3 shows structural results obtained in classical and quantum simulations of SPC/E ice Ih at 220 K. Interestingly, although the classical oxygen-oxygen RDF is very similar to the one obtained in the classical simulation of TIP4P ice,²⁴ the classical oxygen-hydrogen RDF indicates that there are notable differences between the classical TIP4P and SPC/E ices. Indeed, the peaks at about 3.9 and 6.0 Å, clearly noticeable in the classical TIP4P oxygen-hydrogen RDF (see Ref. 24), are much smaller in the classical SPC/E oxygen-hydrogen RDF. The near-neighbor oxygen-oxygen and oxygen-hydrogen distances are still similar to the ones obtained with the TIP4P model and experimentally. As in the TIP4P results,²⁴ the softening of the structure when going from classical to quantum simulations is apparent. It is also evident that the softening of the structure due to quantization extends over many angstroms. The results presented in Fig. 3 are qualitatively similar to the ones obtained by Gai *et al.*¹¹ using path integral Monte Carlo (PIMC) simulations of ice Ih at 240 K with the SPC model.

In Fig. 4, the radial distribution functions obtained in classical and quantum simulations of TIP4P-Ew ice at 220 K are presented. The results are very similar to those obtained

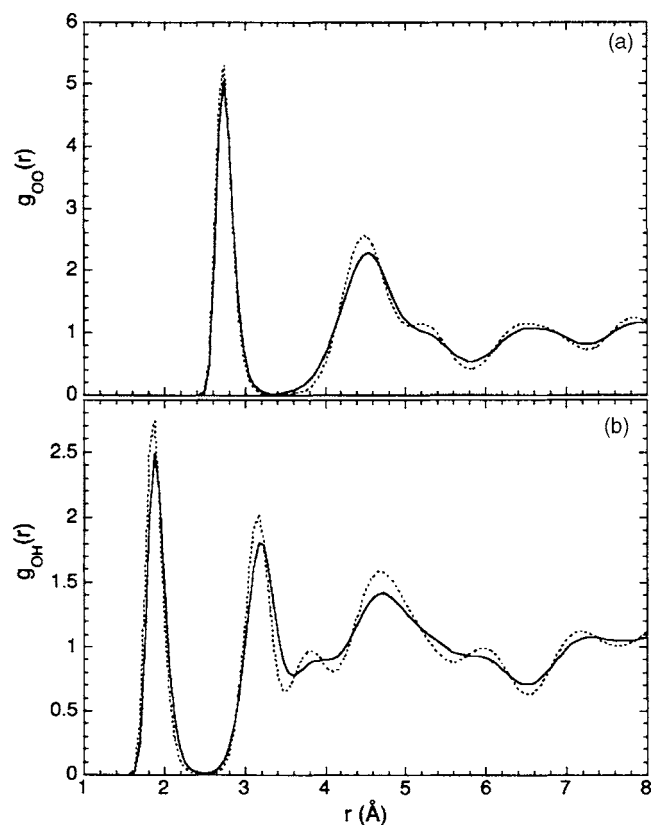


FIG. 4. Oxygen-oxygen (a) and oxygen-hydrogen (b) radial distribution functions of TIP4P-Ew ice Ih at 220 K. The results represented by dotted and solid lines correspond to the classical and quantum simulations, respectively.

with the TIP4P water model.²⁴ The effects of quantization are comparable to those described previously in Fig. 3 and Ref. 24.

A quantitative comparison of the impact of quantization upon simulated ice at 220 K for all three models is presented in Table IV. The TIP4P water model exhibits the largest relative energy shift followed by the TIP4P-Ew and the SPC/E models. These results are in agreement with the observed trends in liquid water at 298 K (see Table I). The molecular uncertainty in ice, calculated with Eq. (38), exhibits somewhat less model dependence than that found in liquid water simulations. It is important to note that the energy shifts and the molecular uncertainties observed for ice are consistently smaller than the corresponding values obtained in liquid phase. According to the results presented and discussed in

TABLE IV. Intermolecular potential energy, relative energy shift, and quantum molecular uncertainty (see text) values for the SPC/E and TIP4P-Ew ice Ih at 220 K. Results for TIP4P (Ref. 24) and PIMC results (Ref. 11) for SPC are included for comparison.

Model	Energy (kJ/mol)		Relative shift (%)	Quantum uncertainty (deg)
	Classical	Quantum		
SPC/E	-55.28	-55.44	5.1	9.8
TIP4P-Ew	-55.48	-55.01	5.9	10.0
TIP4P	-50.84	-47.49	6.6	10.2
SPC	-50.06	-46.0	9	...

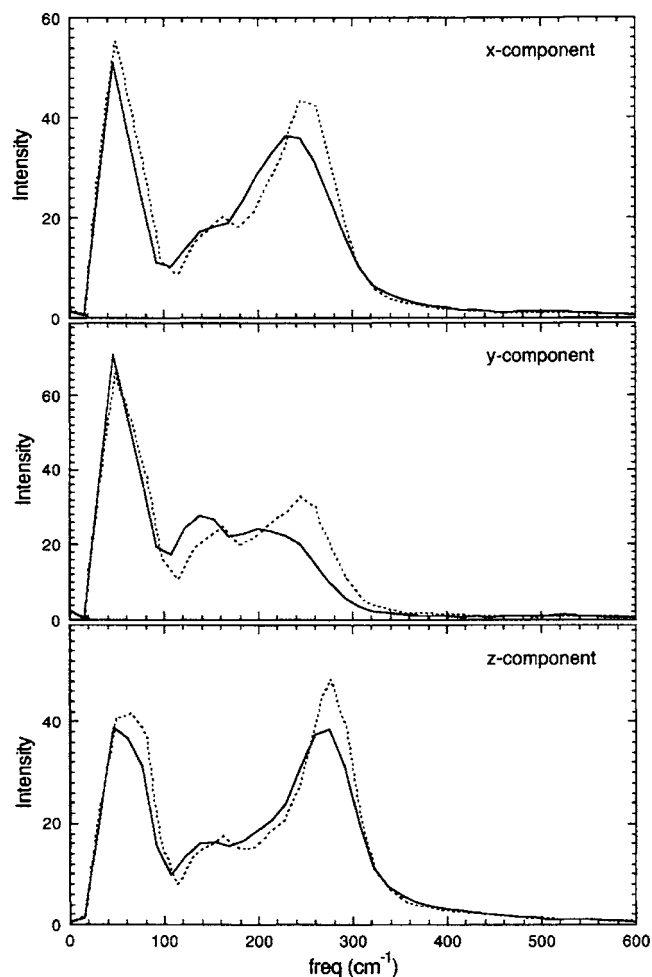


FIG. 5. Fourier transform of the components of the linear velocity time correlation functions for classical and quantum SPC/E ice Ih at 220 K. The results represented by dotted and solid lines correspond to the classical and quantum simulations, respectively. The values of the intensity are arbitrary.

Ref. 23, this is a consequence of the strong interactions between water molecules, which prevents the beads from “taking advantage” of the effective weakening of the harmonic bead-bead interaction implied in the lowering of temperature [first term on the right hand side of Eq. (15)]. We point out that the relative shift in energy obtained from PIMC simulations of the SPC water potential at 220 K by Gai *et al.*¹¹ is larger than the values calculated in this work.

The quantum effects on the lattice vibrations were also examined for the SPC/E and TIP4P-Ew models. The power spectra obtained for classical and quantum SPC/E ices at 220 K are presented in Figs. 5 and 6. Figure 5 displays the power spectra of the components of the linear velocity time correlation functions, whereas Fig. 6 shows the corresponding power spectra of the components of the angular velocity time correlation function. We note that the quantum results in Fig. 6 have been determined from the appropriate centroid time correlation function

$$C_e(t) = \frac{\langle [\mathbf{w}_c(t) \cdot \hat{e}][\mathbf{w}_c(0) \cdot \hat{e}] \rangle_c}{\langle [\mathbf{w}_c(0) \cdot \hat{e}]^2 \rangle_c}, \quad (43)$$

with \mathbf{w}_c and $\hat{e} = \hat{x}, \hat{y}, \hat{z}$ in the local frame, together with Eq. (41). The results are again very similar to those obtained for

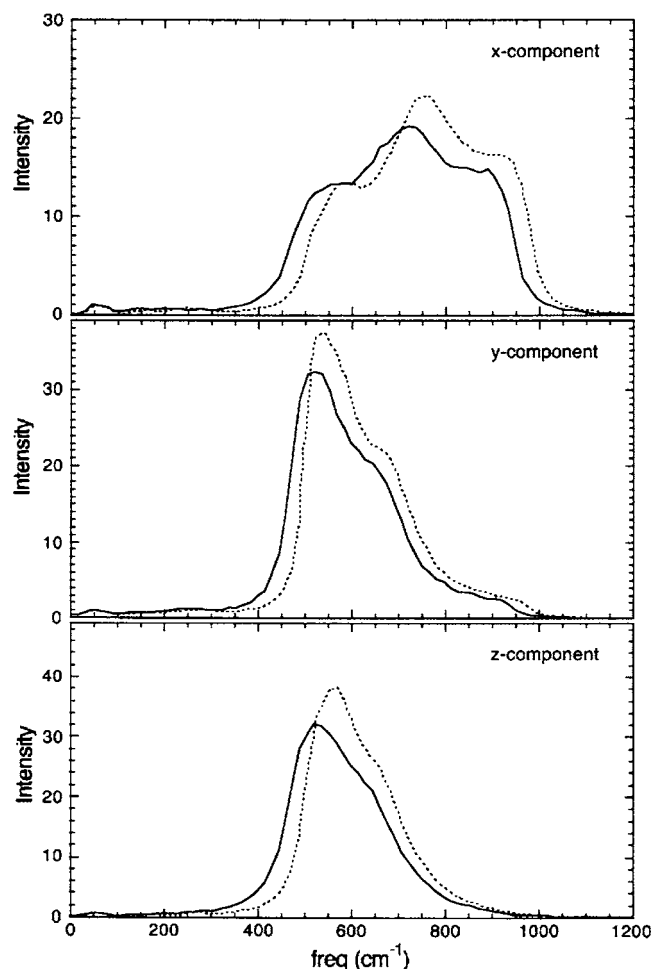


FIG. 6. The power spectra of the components of the angular velocity time correlation functions for classical and quantum SPC/E ice Ih at 220 K. The results represented by dotted and solid lines correspond to the classical and quantum simulations, respectively. The values of the intensity are arbitrary.

the TIP4P model.²⁴ There is a shift to lower frequencies that is much more pronounced in the librational band than the one experienced by the lower frequency modes. The results for the TIP4P-Ew model (not shown) are analogous to the ones presented above and are a further confirmation of the reported behavior.

V. CONCLUSIONS

In this paper we have presented the results of quantum and classical molecular dynamics simulations carried out on liquid water and ice systems with the SPC/E and TIP4P-Ew water models. Some formal and practical considerations in the rigid-body centroid molecular dynamics technique used to perform the quantum simulations in this work have been reviewed. A generalization of the centroid constraint for orientational degrees of freedom is given. We show that this constraint function takes the usual (translational) form when the space curvature becomes negligible. Moreover, in the discretized picture, the centroid constraint can be easily employed to construct orientational paths with the required rotational average by choosing to solve the path integral in centroid frame.

The results from the present rigid-body CMD simulations are compared with those recently obtained for liquid water²¹ as well as ice Ih (Ref. 24) with the TIP4P potential. An energy shift of about 8% and an average molecular uncertainty of about 11° were found independent of the choice of water model. The quantum mechanical uncertainty is consistently smaller in ice Ih than in liquid water for the three models, confirming the importance of the local molecular environment in these properties of liquid water. The dynamical properties of liquid water and ice have also been examined. The self-diffusion coefficient was observed to increase by more than 50% when going from the classical to the quantum system for all the models examined. It was also found that the dynamical isotopic effects are better captured within a quantum dynamical treatment compared to the classical evolution implicit in a standard molecular dynamics simulation. This suggests, in particular, that many of the limitations usually assigned to the parameterization of the molecular models might, in fact, be, predominantly, a consequence of using classical dynamics. Moreover, the present results, together with new x-ray data,³⁷ support recent *ab initio* simulation studies⁴² questioning the relative importance of vibrational motion in the calculation of the bulk properties of water via computer simulations.

Finally, this work verifies the utility of the rigid-body CMD method. Certainly, current empirical potential models for classical simulations of water have the advantage that for large systems they include effects such as quantum delocalization and polarization in an averaged but efficient manner. The large quantum effects found in this and other papers allows one to conclude that to go beyond such effective potentials a consistent improvement of the description of liquid water and ice (through, for example, a more realistic intermolecular interactions derived from *ab initio* electronic calculations) cannot ignore the impact of proton delocalization. In this context, the approximation of rigidity yields a substantial computational advantage while reproducing the experimental isotopic shifts.

ACKNOWLEDGMENTS

The authors are grateful for the financial support of the Natural Sciences and Engineering Research Council of Canada. One of the authors (L.H.d.I.P.) would also like to acknowledge Dr. R. van Zon for useful discussions.

- ¹R. P. Feynman and A. R. Hibbs, *Quantum Mechanics and Path Integrals* (McGraw-Hill, New York, 1965).
- ²R. P. Feynman, *Statistical Mechanics: A Set of Lectures* (W.A. Benjamin, Inc., Reading, MA, 1972).
- ³J. Berne and R. Thirumalai, *Annu. Rev. Phys. Chem.* **37**, 406 (1986).
- ⁴D. Chandler, in *Liquids, Freezing and Glass Transition*, edited by J. P. Hansen, D. Levesque, and J. Zinn-Justin (North-Holland, Amsterdam, 1991).
- ⁵R. A. Kuharsky and P. J. Rossky, *J. Chem. Phys.* **82**, 5164 (1985).
- ⁶A. Walqvist and B. J. Berne, *Chem. Phys. Lett.* **117**, 214 (1985).
- ⁷G. S. del Buono, P. J. Rossky, and J. Schinitker, *J. Chem. Phys.* **95**, 3728 (1991).
- ⁸H. A. Stern and B. J. Berne, *J. Chem. Phys.* **115**, 7622 (2001).
- ⁹J. Lobaugh and G. A. Voth, *J. Chem. Phys.* **106**, 2400 (1997).
- ¹⁰B. Guillot and Y. Guissani, *J. Chem. Phys.* **108**, 10162 (1998).
- ¹¹H. Gai, G. K. Schenter, and B. C. Garret, *J. Chem. Phys.* **104**, 680 (1996).

- ¹²J. Cao and G. A. Voth, J. Chem. Phys. **99**, 10070 (1993).
- ¹³J. Cao and G. A. Voth, J. Chem. Phys. **100**, 5093 (1994).
- ¹⁴J. Cao and G. A. Voth, J. Chem. Phys. **100**, 5106 (1994).
- ¹⁵J. Cao and G. A. Voth, J. Chem. Phys. **101**, 6157 (1994).
- ¹⁶J. Cao and G. A. Voth, J. Chem. Phys. **101**, 6168 (1994).
- ¹⁷S. Jang and G. A. Voth, J. Chem. Phys. **111**, 2357 (1999).
- ¹⁸S. Jang and G. A. Voth, J. Chem. Phys. **111**, 2371 (1999).
- ¹⁹J. A. Poulsen, G. Nyman, and P. J. Rossky, Proc. Natl. Acad. Sci. U.S.A. **102**, 6709 (2005).
- ²⁰L. Hernández de la Peña and P. G. Kusalik, Mol. Phys. **102**, 927 (2004).
- ²¹L. Hernández de la Peña and P. G. Kusalik, J. Chem. Phys. **121**, 5992 (2004).
- ²²L. Hernández de la Peña and P. G. Kusalik, J. Am. Chem. Soc. **127**, 5246 (2005).
- ²³L. Hernández de la Peña, M. S. Gulam Razul, and P. G. Kusalik, J. Phys. Chem. A **109**, 7236 (2005).
- ²⁴L. Hernández de la Peña, M. S. Gulam Razul, and P. G. Kusalik, J. Chem. Phys. **123**, 144506 (2005).
- ²⁵W. L. Jorgensen, J. Chandrasekhar, J. D. Madura, R. W. Impey, and M. L. Klein, J. Chem. Phys. **79**, 926 (1983).
- ²⁶T. F. Miller III and D. E. Manolopoulos, J. Chem. Phys. **123**, 154504 (2005).
- ²⁷H. J. C. Berendsen, J. R. Grigera, and T. P. Straatsma, J. Chem. Phys. **79**, 926 (1983).
- ²⁸H. W. Horn, W. C. Swope, J. W. Pitera, J. D. Madura, T. J. Dick, G. L. Hura, and T. Head-Gordon, J. Chem. Phys. **120**, 9665 (2004).
- ²⁹B. Kuipers, *Quaternions and Rotation Sequences* (Princeton University Press, Princeton, 1999).
- ³⁰S. Buss and J. P. Fillmore, ACM Trans. Graphics **20**, 95 (2001).
- ³¹L. S. Schulman, *Techniques and Applications of Path Integrations* (Wiley, New York, 1981).
- ³²G. J. Martyna and M. L. Klein, J. Chem. Phys. **97**, 2635 (1992).
- ³³A. Dullweber, B. Leimkuhler, and R. McLachlan, J. Chem. Phys. **107**, 5840 (1997).
- ³⁴M. E. Tuckerman, Y. Liu, G. Ciccotti, and G. J. Martyna, J. Chem. Phys. **115**, 1678 (2001).
- ³⁵From Eq. (20) one can show that $0 = \sum_{k=1}^P \{(\mathbf{u}_k \cdot \mathbf{w}_k) \mathbf{u}_k + (\theta_k/2 \sin(\theta_k/2)) \times [\cos(\theta_k/2)(\mathbf{w}_k - (\mathbf{u}_k \cdot \mathbf{w}_k) \mathbf{u}_k) + \sin(\theta_k/2) \mathbf{u}_k \times \mathbf{w}_k]\} \approx \sum_{k=1}^P \{\mathbf{w}_k + (\theta_k/2) \mathbf{u}_k \times \mathbf{w}_k\}$, where the last result is valid for $\theta_k \approx 0$. Thus, for a spherical molecule, Eq. (33) enforces \mathbf{w}_k to be along \mathbf{u}_k ; this approximation resembles the analogous translational problem. One then expect that near to the classical limit the non-Hamiltonian behavior can be neglected.
- ³⁶D. J. Evans and G. P. Morris, *Statistical Mechanics of Non-equilibrium Liquids* (Clarendon, Oxford, 1989).
- ³⁷R. T. Hart, Q. Mei, C. J. Benmore, J. C. Neufeind, J. F. C. Turner, M. Dolgos, B. Tomberli, and P. A. Egelstaff, J. Chem. Phys. **124**, 134505 (2006).
- ³⁸Note that this procedure is identical to computing the mean value of the distribution $p(\theta) = \langle \delta(\theta - \theta_c(\mathbf{R}, \boldsymbol{\Omega}_c)) \rangle_c$, where $\langle \cdot \rangle_c$ is the centroid average performed in Eq. (38); see Refs. 21 and 23.
- ³⁹H. Weingartner, Z. Phys. Chem. (Munich) **132**, 129 (1982).
- ⁴⁰K. Yoshida, C. Wakai, N. Matubayasi, and M. Nakahara, J. Chem. Phys. **123**, 164506 (2005).
- ⁴¹D. Reichman, P. N. Roy, S. Jang, and G. A. Voth, J. Chem. Phys. **113**, 919 (2000).
- ⁴²M. Allesch, E. Schwegler, F. Gygi, and G. Galli, J. Chem. Phys. **120**, 5192 (2004).